Journal of Materials Chemistry A

# Mixed Anion Effects on Structural and Electrochemical Characteristics of $Li_4Ti_5O_{12}$ for High-rate and Durable Anode Materials

| | |
|---|---|
| Journal: | *Journal of Materials Chemistry A* |
| Manuscript ID | TA-ART-06-2023-003494.R4 |
| Article Type: | Paper |
| Date Submitted by the Author: | 23-Dec-2023 |
| Complete List of Authors: | Kim, Hye-min; Shinshu University, Department of Materials Chemistry<br>Kim, Dae-wook; KITECH, Ulsan Regional Division<br>Hara, Kenjiro ; Shinshu University Graduate School of Engineering Faculty of Engineering<br>Shiiba, Hiromasa; Shinshu University, Department of Materials Chemistry<br>Charles-Blin, Youn; Shinshu University Faculty of Engineering, Materials Chemistry<br>Otal, Eugenio; Shinshu University - Ueda Campus, Department of Chemistry and Materials<br>Tanaka, Hideki; Shinshu University, Research Initiative for Supra-Materials<br>Teshima, Katsuya; Shinshu University, Department of Materials Chemistry; Shinshu University, Center for Energy and Environmental Science<br>Sánchez-Santolino, Gabriel; The University of Tokyo, Institute of Engineering Innovation<br>Ishikawa, Ryo; Saitama University, Functional Materials Science<br>Ikuhara, Yuichi; The University of Tokyo, Institute of Engineering Innovation, School of Engineering; Japan Fine Ceramics Center, Nanostructures Research Laboratory<br>Zettsu, Nobuyuki; Shinshu University Graduate School of Engineering Faculty of Engineering, Materials Chemistry |
| | |

ARTICLE

# Mixed Anion Effects on Structural and Electrochemical Characteristics of $Li_4Ti_5O_{12}$ for High-rate and Durable Anode Materials

Received 00th January 20xx,
Accepted 00th January 20xx

DOI: 10.1039/x0xx00000x

Hye-min Kim[a,‡], Dae-wook Kim[a], Kenjiro Hara[a,‡], Hiromasa Shiiba[b], Youn Charles-Blin[a,‡], Eugenio Otal[a], Hideki Tanaka[b], Katsuya Teshima[a,b], Gabriel Sánchez-Santolino[c], Ryo Ishikawa[c], Yuichi Ikuhara[c], and Nobuyuki Zettsu[* a,b,d]

Lithium titanate ($Li_4Ti_5O_{12}$ or LTO) is a zero-strain lithium-insertion anode that experiences no volume change during the charge–discharge cycles. Combining experimental and computational approaches, this study reveals that the exceptional rate capability and cyclability of LTO anodes can be achieved through the utilization of mixed-anion materials, which may possess fundamentally distinct kinetic mechanisms compared to oxides. By incorporating halogen ions ($F^-$, $Cl^-$), electron conductivity is enhanced via d-electron doping. Additionally, the repulsion between $Li^+$ ions in the transition state and the alteration in Li's coordination number significantly affects the energy profile of $Li^+$ ion diffusion along the most energetically favorable pathway in the LTO lattice. Notably, $F^-$ or $Cl^-$ doping on the LTO surface significantly reduced the presence of pentacoordinate Ti atoms on the surface due to halide bonding, resulting in mitigation of electrode deformation due to gas evolution, which is a typical characteristic of LTO electrodes. These novel insights offer new avenues for discovering high-rate electrode materials capable of delivering high cyclability.

## Introduction

The main text of the article should appear here with headings as appropriate. Lithium-ion batteries (LIBs) have experienced considerable success and are now being commercialized for a diverse range of applications. However, increasingly demanding requirements often surpass the capabilities of existing LIBs. This is especially evident in the need for high charge power density to reduce refuelling times for electric vehicles (EVs) and hybrid vehicles (HEVs). Due to safety concerns stemming from dendrite formation, the widely used graphite anode cannot fulfil the high charge power-density requirements.[1,2]

Lithium titanate is a promising material for these applications as it enables rapid charging without Li plating or significant volume expansion, ensuring enhanced safety.[3,4] The zero-strain property of this material arises from a two-phase process involving an initial disordered spinel phase $Li_4Ti_5O_{12}$ (LTO, space group: *Fd*-3*m*) and a rock-salt phase $Li_7Ti_5O_{12}$ (space group: *Fm*-3*m*).[5-7] Although the LTO phase exhibits high $Li^+$ ion mobility during lithiation on a macroscopic scale, lithium insertion into 16c sites and simultaneous $Li^+$ migration to 8a sites are hindered by the poor $Li^+$ mobility of the initial and final phases ($\sigma Li = 10^{-9}$–$10^{-16}$ $cm^2$ $s^{-1}$).[8-10] However, intermediate states ($Li_{4+x}Ti_5O_{12}$, $0 \le x \le 3$) display considerably better $Li^+$ ion diffusivity, particularly in the early stages (from $x$ = 0.1 to $x$ = 1.0).[11] Gaining a comprehensive understanding of the lithiation mechanism and kinetics is challenging.

Numerous strategies have been developed to enhance both electron and $Li^+$ ion conductivities within the LTO lattice. The most prevalent approaches involve reducing particle size to the nanoscale[12-14] or coating the surface with a conductive material.[15-18] The incorporation of foreign atoms through doping has also been extensively explored, using a wide variety of elements. In the literature, transition metals are doped into cationic sites, such as $Mg^{2+}$,[19] $Ca^{2+}$,[20] $Zn^{2+}$,[21] $Cr^{3+}$,[22] $Al^{3+}$,[23] $La^{3+}$,[24] $Zr^{4+}$,[25] $V^{5+}$,[26] $Nb^{5+}$,[27] $Ta^{5+}$,[28] and $Mo^{5+}$,[29] or anions, such as $Br^-$,[30] $N^{3-}$,[31] $Cl^-$,[32] $F^-$[33-36], or $I^-$[37]. For example, doping with divalent Mg ions leads to the reduction of $Ti^{4+}$ to $Ti^{3+}$, enhancing conductivity.[38] The formation of mixed-valence $Ti^{4+}/Ti^{3+}$ can also be achieved through self-doping with $Ti^{3+}$ or by creating oxygen vacancies, which improve the intrinsic conductivity of LTO without introducing impurities.[39, 40] Furthermore, H. Yan et al reviewed current progresses on the representative doped $Li_4Ti_5O_{12}$ with various cations/anions in the Li, Ti and O sites.[41]

Recently, Ceder *et al*.[42] provided a deeper understanding of the intricate $Li^+$ migration mechanism and offered insights into designing electrode materials for fast-charging batteries. They described Li-ion migration through the LTO lattice as a series of

[a] *Department of Materials Chemistry, Shinshu University, 4-17-1 Wakasato, Nagano, 380-8553, Japan.*
[b] *Research Initiative for Supra-Materials, Shinshu University, 4-17-1 Wakasato, Nagano, 380-8553, Japan.*
[c] *Institute of Engineering Innovation, The University of Tokyo, Bunkyo, Tokyo 113-8656, Japan.*
[d] *Energy Landscape Architectonics Brain Bank, Shinshu University, 4-17-1 Wakasato, Nagano, 380-8553, Japan.*

† Footnotes relating to the title and/or authors should appear here.

Electronic Supplementary Information (ESI) available: Models for the DFT calculation, XPS, XRD patters, Charge-discharge profiles, Table of calculated formation energies, and Nyquist plots, details of any supplementary information available should be included here. See DOI: 10.1039/x0xx00000x

bottlenecks, each with numerous activation barriers to overcome. Key factors such as $Li^+$-$Li^+$ repulsion in transition states and the coordination number of Li were identified as greatly influencing the energy profile of $Li^+$ ion diffusion in LTO. Consequently, we employed an anion exchange strategy to substitute LTO oxygen with halogen atoms like fluorine or chlorine under controlled conditions. Replacing oxide ligands in coordination octahedra or tetrahedra with other anions can differentiate the binding energy, which may benefit chemical reaction and anionic diffusion. Furthermore, the crystal field splitting can be tuned to the extent that is only allowed in coordination complexes, while retaining the original polyhedral shape and connectivity.[43] Our goal was to facilitate $Li^+$ ion migration through transition state bottlenecks, thereby enhancing both the kinetics and cyclability of LTO. Due to their atomic radii and electronegativity, the doped atoms are expected to induce deformation of the diffusion bottlenecks. Furthermore, incorporating fluorine or chlorine into the LTO lattice could result in mixed-valence or Li defect formation for crystal neutrality, potentially improving conductivity and reducing $Li^+$-$Li^+$ repulsion.

In this work, we address the discovery of the full picture of the effect of halide anion doping in LTO materials using experimental and theoretical approaches, including X-ray Absorption Fine Structure (XAFS) and atomic-resolution annular dark field (ADF) STEM. In fact, we evaluated the impact of halogen doping (F, Cl) on the structural characteristics, electrochemistry for long-term cycling at high C rates, and kinetic properties of LTO. F- or Cl-doped LTO were synthesized through a controlled carbothermal reaction using amorphous heterocarbon nanoparticles derived from fluorobenzene and chlorobenzene in a solution plasma. To complement our experimental investigation, we further employed first-principles simulations to examine the effects of halogen doping on Li diffusion and surface structure stability. Density Functional Theory (DFT) serves as a powerful tool for predicting lithium diffusion pathways in the LTO phase.[7, 40] We analysed in detail the five-coordinate $Ti^{4+}$ on the LTO surface in XAFS measurements and the $Ti^{3+}$ formed on the surface in STEM observations, and found that these have a significant influence on the electrochemical properties of the LTO. Furthermore, many fundamental studies have been carried out on cation-substitution effects[19-29, 38], but there are only a few reports on mixed-anion effects.[30-38] Therefore, determining the full picture for mixed-anion effects of spinel lithium titanate systems provides new methods for material design that overcome the current performance limitations. We believe that LTO contained in batteries implemented so far has been used with a lower active material weight ratio and further limited to a very narrow state of charge (SOC) range to avoid the above gas evolution problem and low electronic conductivity problem. We believe our findings will lift these use restrictions and provide LTO-related compounds that can be used in a wider range of SOC conditions.

## Experimental

**Synthesis of F-, Cl- doped heterocarbon nanoparticles**

F- or Cl- doped amorphous hydrocarbon (F-HC and Cl-HC) powders were synthesized using the solution plasma process (SPP). The formation of amorphous nanocarbon powder with a disordered phase occurred due to nonequilibrium cold plasma in an aryl halide solvent.[44] Fig. 1 illustrates a schematic diagram of the SPP setup. In this study, 80 mL of fluorobenzene ($C_6H_5F$) or 80 mL of chlorobenzene ($C_6H_5Cl$) was utilized as the precursor for synthesizing each type of heterocarbon particle. A bipolar pulsed generator (Kurita Manufacturing Co., Ltd., MPP04-A4-30) served as the power supply for the glow discharge within the solvent. The applied voltage and pulse width were set at 1.6 kV and 2 μs, respectively. The resulting suspension was filtered and dried in a vacuum oven at 100 °C. After discharging for 1 h, approximately 1 g of black powder was obtained.

**Synthesis of LTO single crystal**

LTO crystals were prepared through flux growth using a LiCl-KCl mixed molten salt. [45] Reagent-grade $Li_2CO_3$, $TiO_2$, KCl, and NaCl (Wako Pure Chemical Industries, Ltd.) were employed for growth. A stoichiometric mixture of $Li_2CO_3$ (2.8 g) and $TiO_2$ (7.7 g) powders was used as the solute, while NaCl (0.34 g) and KCl (0.82 g) powders were utilized as fluxes. All mixtures were placed in 30 $cm^3$ crucibles. After loosely closing the lids, the crucibles were positioned in an electric furnace, heated to 800 °C at a rate of 700 °C $h^{-1}$, and maintained at the target temperature for 10 h. Subsequently, the samples were cooled to 500 °C at a rate of 200 °C $h^{-1}$, controlled by a cooling program and allowed to cool to room temperature within the furnace. The excess flux was thoroughly removed from the product by rinsing it with water.

**Synthesis of F-, Cl-doped FLTO single crystal**

A mixture of 0.015 g of HC powders and 0.5 g of LTO powders was heated at 600 °C for 3 h in air. Two different LTO powders were used for synthesis: a kaolinized LTO powder purchased from Hosen Co. Ltd. (Japan) and an LTO single crystal grown from a molten salt of the NaCl-KCl mixture (as described earlier).

**Atomic-resolution scanning transmittance electron microscopy**

The atomic and electronic structures on the surfaces were characterized using atomic-resolution scanning transmission electron microscopy (STEM) combined with electron energy-loss spectroscopy (EELS). LTO powders were dispersed in ethanol and placed on a perforated amorphous carbon grid supported by a copper mesh. Atomic-resolution annular dark-field (ADF) STEM images were obtained by a JEM ARM300CF (JEOL, Ltd.). This electron microscope is equipped with a cold-field emission gun, a delta-type aberration corrector, and a EEL spectrometer (Quantum ER, Gatan Inc.). The convergence semi-angle was set to 30 mrad, and the collection semi-angle for ADF-STEM ranged from 72 to 200 mrad. To minimize beam irradiation damage to the LTO, the microscope was operated at 80 kV with a relatively low beam current of approximately 10

pA. Under the observation condition, no significant structural changes were observed during image acquisition. For spectrum imaging, the electron beam is scanned along the region of interest and an EEL spectrum is acquired in every pixel. To quantify the titanium oxidation state, we performed a multiple linear least square fit (MLLS) of the Ti $L_{2,3}$ edge to two reference spectra for bulk $LaTiO_3$ ($Ti^{+3}$) and $SrTiO_3$ ($Ti^{+4}$), allowing us to map the oxidation state for every probe position.[46]

#### X-ray absorption fine-structure spectroscopy

Ti *K* edge X-ray absorption fine-structure spectroscopy (XAFS) spectra of LTO, F-LTO, and Cl-LTO powders were measured to evaluate their x-ray absorption near-edge structures (XANES), which contains information about bond distances and bond angles around the absorbing Ti atom, as well as about its oxidation state. XAS measurements were performed at Aichi Synchrotron Radiation Center. Measurements were performed in QXAS mode at the Ti K-edge (4966 keV). Surface-sensitive measurements were performed at BL6N1 using Conversion Electron Yield (CEY) under helium atmosphere. Samples were attached to carbon tape and a bias voltage of +150 V was applied to a Cu-grid in front of the sample holder. Bulk measurements were performed in transmission mode at BL11S2. Samples were diluted with BN in glove box and packed under argon in aluminized bags with Kaptoin windows. Helium gas was used in the incident beam to the incident ionization chamber. Peak deconvolution was performed using gaussian functions. A2 peak intensity was normalized to the sum of A1-A3 and B peaks.

#### Electrochemical characterization

The electrochemical properties were assessed using an R2032-type coin cell. The cathode comprised active materials, acetylene black, and polyvinylidene fluoride (PVDF) in a weight ratio of 90:5:5. The resulting paste was applied to 20 µm-thick aluminum foil using a Baker applicator. All electrodes were dried at 120 °C in a vacuum for 24 hours before use. The loading amount of active materials and the electrode density were controlled at 2.0 mg/cm$^2$ and 2.1 g/cm$^3$, respectively. A porous polypropylene film (#2500, Celgard) served as the separator. The electrolyte was a 1 M $LiPF_6$ solution mixed with ethylene carbonate and dimethyl carbonate at a 3:7 volume ratio. The 2030-type coin cells were assembled in an argon-filled glovebox (MDB-2BL; Miwa Mfg Co., Ltd., Japan) under a controlled atmosphere (≤1 ppm of H2O and O2). Galvanostatic charge-discharge tests were conducted using a galvanostat (HJ1020Msd8, Hokuto Denko, Japan) with a voltage range of 3.5–4.8 V (vs $Li^+$/Li). Electrochemical impedance spectroscopy (EIS) and cyclic voltammetry (CV) measurements were performed using an electrochemical workstation (VSP-300, Bio-logic, France). The EIS frequency range was 200 kHz to 1 MHz, while the CV voltage range was 1.0–2.0 V at a scan rate of 0.1 mV· s$^{-1}$. All electrochemical measurements were carried out in a temperature-controlled chamber (SU-221, Espec, USA) set at 25 °C.

#### DFT calculation

DFT calculations were performed using the generalized gradient approximation (GGA-PBEsol) + U and projector-augmented wave methods implemented in the Vienna ab initio simulation package (VASP).[47-49] The U values of the d-orbitals of Ti were set to 4.2 eV.[50-52] An energy cutoff of 500 eV and a 1 × 1 × 1 k-point mesh were utilized for the 84-atom superstructure in a cubic spinel lattice of $Li_{16}Ti_{20}O_{48}$ with *Fd*-3*m* symmetry as the starting structure. To achieve the atomic arrangement of 8($Li_4Ti_5O_{12-x}A_x$) ($x$ = 0.25, 0.50, 0.75, and 1.00), one to four halide anions were added to the possible 32e oxygen sites in the unit cell. The nudged elastic band method was employed to examine the minimum energy pathways of lithium hopping between adjacent lattice positions.[53-55] Crystal structure relaxation was allowed for all calculations, and the final energies of the optimized geometries were recalculated to account for changes in the plane-wave basis during relaxation. To compute the energy of a slab with a surface facet, atoms on the LTO surface were manually arranged while preserving their crystallographic symmetry and chemical stoichiometry. The top and bottom slab surfaces' crystallographic symmetries were crucial for accurate computational predictions. Slab cells were constructed from a relaxed bulk structure, with lattice parameters fixed to the slab cells. For surface facet calculations, slab thicknesses exceeding 20 Å (surface region: 5 Å, bulk layer: 10 Å) were selected for all facets, with vacuum thicknesses of 10 Å (Fig. S1).

## Results and discussion

#### Structural characterization

Fig. 1 summarizes the halide anion ($F^-$ or $Cl^-$) doping into the spinel $Li_4Ti_5O_{12}$ (LTO) crystal surface, achieved through a carbothermal reaction using F-HC, Cl-HC particles. Both F-HC and Cl-HC particles were synthesized via a solution plasma process (SPP) using aromatic halides (fluorobenzene and chlorobenzene) as raw materials. A nonequilibrium cold plasma discharge in a mixture of benzene and fluorobenzene or chlorobenzene resulted in the formation of black powders. FE-SEM observations revealed that the black particles formed spherical shapes with diameters ranging from 20 to 30 nm. Powder XRD profiles suggest that the particles formed an amorphous phase (Fig. S2(a), (b)). The chemical composition, including oxygen, fluorine, and chlorine contents in atomic percentages, was determined using XPS (Fig. S2(c), (d)). Approximately 2 at% of the halides were incorporated into the amorphous carbon matrix. As reported in previous studies, high amounts of hydrogen were also present in the matrix, indicating that the F-HC and Cl-HC particles facilitated combustion in the subsequent reaction under air at high temperatures.

After the carbothermal reaction, the LTO powders turned light bluish-white, regardless of the halide anions involved (Fig. 1). Such color change strongly suggests the $Ti^{3+}$ is preferentially formed in the LTO framework, over Li deficient formation or LiF deposition.[35] The XPS spectra reveal a distinct surface chemical environment due to the incorporation of halide anions into the LTO lattice. Fig. 2 presents the spectra recorded for commercial

LTO powder and the corresponding fluoride-anion-doped LTO (F-LTO) and chloride-anion-doped LTO (Cl-LTO) powder samples. The F1s XPS spectrum of F-LTO in Fig. 2(a) displays an asymmetric peak characteristic of F in various bonding states. After curve-fitting, the F 1s peak can be deconvoluted into single peak at binding energies of approximately 684.0 eV, attributable to Ti-F bonds.[35] The broad Cl2p peak observed in the Cl-LTO powder signifies the 2p1/2 and 2p3/2 peaks, located at 199.0 and 197.3eV, attributable to Ti-Cl-Ti and Ti-Cl bonds, respectively.[56] These results confirm the successful doping of $F^-$ or $Cl^-$ within the LTO matrix through the carbothermal reaction. To determine the chemical composition related to the halide anion doping level, depth profile measurements using XPS were conducted for both F-LTO and Cl-LTO powders. Figs. 2(c) and (d) display the F 1s and Cl 2p spectra recorded at various depths from the surface. In all cases, the F 1s and Cl 2p signals significantly weakened at a depth of 20 nm, but they did not completely disappear at a depth of 100 nm. This suggests that the doped halide ions were concentrated near the particles and decreased with increasing depth. The changes in the structural and electrochemical characteristics of the doped halide anions were more prominent in the particle surface layer, which might be due to the rapid reaction during the brief carbothermal processes. The contents of O and F were evaluated using core-level X-ray photoelectron spectroscopy (XPS). The atomic ratios of F to O and Cl to O were estimated to be 1.72:100 and 1.07:100, respectively. Based on these values, the molecular formulae formed near the top layer were determined to be $Li_4Ti_5O_{11.26}F_{0.19}$ and $Li_4Ti_5O_{11.26}Cl_{0.16}$, respectively.

The incorporation of F- or Cl- anions and the generation of $Ti^{3+}$ enhanced the electronic conductivity and electrochemical characteristics. High-resolution Ti 2p spectra (Fig. 2(e)) are displayed for LTO (top), F-LTO (middle), and Cl-LTO (bottom). Specifically, the peaks corresponding to the LTO particles align well with the Ti 2p1/2 and Ti 2p3/2 peaks of tetravalent Ti ($Ti^{4+}$). In contrast, both F-LTO and Cl-LTO exhibit a slightly lower energy shift for the Ti 2p1/2 and Ti 2p3/2 peaks related to the $Ti^{4+}$ peaks, indicating the presence of mixed valence states of $Ti^{4+}$ and trivalent ($Ti^{3+}$), the latter of which is known to increase electron conductivity via *d*-electron doping ($[Ar]3d^1$). The difference spectrum obtained by subtracting the normalized Ti 2p spectrum of F-LTO and Cl-LTO from that of pristine LTO contains two positive peaks at approximately 463.2 and 457.6 eV assigned to $Ti^{3+}$ and two valleys at 464.9 and 458.9 eV assigned to $Ti^{4+}$, respectively (Fig. S3).[35, 57] The depth profiles of XPS Ti 2p spectra were further conducted, and as shown in Fig. 2 (f), the peak shift to the lower energy side caused by the halide ion substitution tended to return to the original position with increasing depth. Taken together, these results suggest the formation of $Ti^{3+}$ states at the expense of $Ti^{4+}$ in the LTO lattice via charge compensation after the incorporation of halide ions. Fig. 3(a) displays the powder XRD patterns of F-LTO, Cl-LTO, and pristine LTO crystals. Despite the incorporation of halide ions, the diffraction profiles remained largely unaltered. The diffraction lines corresponded to a cubic spinel structure belonging to the *Fd*-3*m* space group (ICDD# 00-0026-1198), with no detected impurity phases. This suggests that doping did not cause any noticeable structural changes in LTO. However, the peak positions exhibited minor shifts toward lower angles upon anion doping. For example, the peak at $2\theta = 18.4$, assigned to the 111 faces, is demonstrated in Fig. 3(b). The lattice parameters experienced slight shifts as well, from 8.3508 Å in the pristine sample to 8.3575 Å for F-LTO and finally to 8.3590 Å for Cl-LTO powders. We propose that the observed lattice parameter expansions in F-doped LTO and Cl-doped LTO are not solely attributed to the substitution of anions with varying ionic radii ($F^-$: 1.33 Å, $Cl^-$: 1.81 Å, $O^{2-}$: 1.40 Å). Instead, they likely result from a combination of factors, including lattice expansion due to the formation of $Ti^{3+}$ or $Li^+$ defects arising from charge-compensation reactions.

The morphologies of the pristine LTO, F-LTO, and Cl-LTO crystals were examined using FE-SEM. Fig. 3(c-e) illustrates that the pristine LTO crystals exhibit irregular shapes and a crystal size ranging from a few hundred nanometers. When compared to the pristine LTO crystals, the halide anion-doped LTO crystals displayed minor changes in morphology while maintaining a similar average size, potentially due to alterations in surface energy. To better visualize the subtle changes in crystal morphology for LTO particles with irregular shapes, the carbothermal reaction was applied to well-defined octahedral LTO single-crystal particles, which were grown from molten LiCl-KCl mixed salt. Comparable results were observed in the irregularly shaped particles concerning their changes in collar. Chemical environments, based on XPS spectra (Fig. S4) and XRD profiles (Fig. S5), were also detected in the LTO single-crystal particles due to the incorporation of halide anions. In the experiment using single crystal LTO, more halide ions were substituted than those doped in the LTO particles (Fig. 3), so that the particle morphology change caused by halide ions substitution can be clearly seen. As, expected, notable changes in crystal morphology were observed using FE-SEM. As demonstrated in Fig. S6, halide anion doping facilitated the transition at the edges and corners of the well-defined octahedral LTO crystals.

Morphological changes exhibited by crystals in which halide ions were replaced by the combustion reaction of heterocarbons were similarly observed in LNMO crystals.[59, 60] In other words, we were able to predict in advance that the change in crystal habit via the halide ion substitution would occur. On the other hand, a different behaviour was observed in LTO crystals in which fluoride ions were substituted at the atomic level using $XeF_2$.[35, 36] According to Louvain group reports, the nanometer-sized LiF particle are deposited on the surface of F-LTO crystals. It has not led to changes in crystal habit as we report in this manuscript. We understand this is because their reports are reactions that proceed at room temperature. The oxidation force of $XeF_2$ is so strong that some of the oxide ions are undoubtedly replaced by fluoride ions in the lattice near the surface of the LTO particles. However, the formation of the deposits suggests that the solubility problem may greatly limit the amount of substitution in the case of anion doping at room temperature. In other words, it is highly likely that the excess fluoride ion substitution beyond the limit of solid solution promoted Li-F bonding with Li inside the crystal, resulting in the

particle exiting through phase separation. Since the deposit on such fine particles has the effect of suppressing the high resistance due to the decrease of the specific surface area for the reaction and the decomposition of the electrolyte, our method contains a large gain in strictly discussing the effect of halide ion substitution on the structure and electrochemical features.

This is most evident in the atomic-resolution annular dark-field (ADF) STEM image of the Cl-LTO viewed along the [110] orientation, as shown in Fig. 4(a). The particles have two stable facet planes of {100} and {111}, which is well consistent with the FE-SEM observations. The formation of the large face planes suggests that the halogen stabilizes the {110} facet and promotes its formation. On a closer examination of the topmost surface, no antisite defects between transition metals and Li were detected in its atomic structure, as shown in Fig. 4(b), and Fig. S7. Unlike Cl-LTO, a disrupted atomic structure (antisite defect) on the surface in F-LTO was observed, where the thickness was only a few atomic layers from the surface. F-LTO is more inclined to form a $Li^+$-deficient phase in the outermost surface layer rather than a $Ti^{3+}$ phase.

Fig. 4(c) and (d) show the oxidation state of Ti in F-LTO and Cl-LTO as a function of distance from the surface, respectively, where the oxidation state was evaluated from the Ti-$L_{2,3}$ edges by EELS. Near the surface regions, the Ti oxidation state is significantly reduced to 3+ in both samples, and the reduced thicknesses are estimated to be 2 nm for F-LTO and 10 nm for Cl-LTO, respectively. The spatial distribution of the Ti oxidation state in Cl-LTO is given in Fig. 4(e). Since the amount of doped $F^-$ or $Cl^-$ ions in LTO is considerably small, it is challenging to obtain elemental signals in EELS. However, to maintain the charge neutrality, the observed Ti reduction at the surface region could contain some amounts of $F^-$ or $Cl^-$ ions at the oxygen sites within a few nanometers from the surface.

**X-ray absorption fine-structure spectroscopy**

X-ray absorption spectroscopy measurements were carried out in order to clarify the effect of halide doping on the chemical states of LTO. Fig 5(a) shows the Ti K-edge XANES spectra of the LTO samples collected in CEY mode, which are sensitive to only a few tenths of nanometers from the surface of the particles. The three spectra show no differences in the XANES spectra, indicating the environment of the Ti atoms is similar among the samples, the inset also shows that the intensity of the white line is not modified. The Radial Function Distribution (Fig 5(b)) shows an increase of the first coordination shell in Cl-LTO and F-LTO samples with respect to LTO, this can be related to an increase of the coordination number of Ti atoms in treated samples.

Fig 5(c) – (e) displays the deconvolution of Ti pre-edge peaks. The distinct features observed in the A1-A3 and B peaks in the pre-edge region can be attributed to the influential polarization of the p-orbitals and the substantial mixing of p and d orbitals during the 1s-3d transitions. Using the monoelectronic approximation, the pre-edge peak transitions were accurately identified with certainty.[58] The A1 peak primarily arises from a dipolar on-site transition to a final state where 4p and 3d orbitals are hybridized, A2 is related to pentacoordinate Ti atoms, A3 peak results from a mix of dipolar transitions to hybridized 4p–3d states, influenced significantly by the strong hybridization with the 3d orbitals of the closest Ti atom, along with a minor quadrupolar component and, B peak is exclusively dipolar, characterized by an off-site transition where the electron's final state is spread out around the absorbing atom.[58, 61] The normalized intensity of peak A2 for the TLO samples is plotted in Fig. 5(f). The intensity of A2 shows a strong intensity reduction after the carbothermal reaction. This peak intensity reduction can be related to the fulfilment of octahedral coordination of pentacoordinate Ti due to the halide bonding after HC treatment and it is in agreement with the change in intensity of the first coordination shell in Fig. 5 (b)

**Electrochemical characterization**

Cyclic voltammetry was conducted on cells containing pristine LTO, F-LTO, and Cl-LTO electrodes within a voltage range of 1.0-2.0 V (vs. $Li/Li^+$) at scan rates of 0.2 $mV{\cdot}s^{-1}$ (Fig. 6(a)). Both F-LTO and Cl-LTO exhibited smaller peak current separations ($\Delta E_p$) of 0.087 and 0.084 V in the first cycle compared to that of pristine LTO (0.133 V). Moreover, an effect of halide ion incorporation on the lithiation voltage was observed in the lithiation process for pristine LTO. Fig. 6(b) displays the reversible discharge capacities of pristine LTO, F-LTO, and Cl-LTO at a 0.2 C rate. The lithiation process was exothermic, with an average voltage of 1.52 V. Both F- or Cl-doping made the lithiation process more favourable, resulting in an increased voltage of 1.57 V. This observation can be ascribed to improvements in the kinetic parameters related to lithium-ion diffusion characteristics and the relatively stable performance of F-LTO and Cl-LTO, which are consistent with the subsequent rate performance tests.

Assuming a three-electron reduction per formula unit, F-LTO and Cl-LTO are expected to have a slightly lower theoretical capacity compared to LTO due to $Ti^{3+}$ formation through charge compensation by halide ion incorporation. However, at low current densities, both pristine LTO and Cl-LTO displayed similar capacities of approximately 155 mAh $g^{-1}$, while F-LTO exhibited lower capacities ranging between 145 and 150 mAh $g^{-1}$. The theoretical capacity (determined by the constraints of the crystal structure) is 175 mAh/g if lithium ions are inserted only at the 16c site, however in practice, Li ions can also be occupied at the 8a site. It is quite difficult to achieve theoretical capacity in LTO where lithium- ion insertion/deinsertion proceeds in a two-phase reaction mechanism rather than a simple solid-solution reaction. The differences between experimental results and what is predicted by theory are discussed that the presence of $Ti^{3+}$ can improve access to active site, and then can increase the specific capacity of the material compared to the pristine one. Other reports have also shown that halide-ion-substituted LTOs have higher specific capacities than pristine LTOs, although only below the theoretical capacity.[30-37] Furthermore, the capacity reduction in F-LTO, as comparing to Cl-LTO may stem from slightly degraded electronic conductivity,

which can be attributed to the strong electronegativity of fluorine.

Fig 6 (c). illustrates the representative effects of halide ion doping on the rate capability of LTO electrodes, with Cl-LTO consistently delivering higher capacities than both pristine and F-LTO at 0.2, 0.5, 1, 5, 10, and 20 C within the 5th, 10th, 15th, 20th, 25th, and 30th cycles, respectively. The improved performance of Cl-LTO was most prominent at higher rates, akin to previous reports for related Br-doped LTO systems.[30] It is plausible that Cl-LTO may deliver higher capacity due to the substitution of $O^{2-}$ with $Cl^{-}$, causing a portion of $Ti^{4+}$ to become $Ti^{3+}$ because of charge balance considerations. These effects would increase the material's electrical conductivity, which is consistent with the XPS measurements. F-LTO yielded intriguing results. It exhibited the lowest discharge capacity at slower discharge rates; however, its capacity retention with increasing discharge rates was similar to that of Cl-LTO. Above 10C, the discharge rates of F-LTO electrodes displayed a reversal phenomenon, and F-LTO delivered slightly higher capacities than the corresponding pristine LTO. The improved Li diffusion properties induced by doping allowed both F-LTO (110 mAh g-1) and Cl-LTO (115 mAh $g^{-1}$) to provide enhanced outputs compared to bare LTO (103 mAh $g^{-1}$).

The galvanostatic charge-discharge profiles for 1C, 10C, and 20C rates for pristine LTO, F-LTO, and Cl-LTO are displayed in Figs. 6(d)-(f), respectively, revealing plateaus associated with stable $Ti^{4+}/Ti^{3+}$ reduction. The obtained charge-discharge profiles did not show significant differences in the voltage plateaus related to the redox reaction for all electrodes. This suggests that no subphase was formed during the anion doping process, which is in line with the XRD analysis results. However, notable differences were observed in the specific capacity and polarization at various C-rates (Fig. S8). The polarization of the cells increased with the current density, as indicated by the open charge/discharge galvanostatic curves. This demonstrates that F-LTO and Cl-LTO consistently exhibit lower polarization due to their less resistive interfaces (Fig. S9). Both $F^{-}$ or $Cl^{-}$ doped LTO-based electrodes displayed improved intercalation properties, which supports the peak separations between the cathodic and anodic waves observed in the CV measurements. This difference in functional capacity is ascribed to the enhanced electronic and ionic access of F- or Cl-doped LTO.[62-64] Specifically, the corresponding increase in $Ti^{3+}$ allows for greater electronic conductivity. This factor contributes to more redox-active sites being accessed electrochemically, resulting in an increase in capacity.

The kinetic parameters were evaluated using electrochemical impedance spectroscopy (EIS) (Fig. S10). The Nyquist plots of the LTO electrodes obtained after aging for three cycles at 0.2C were fitted to the circuit shown in Fig. S10. $R_s$ represents the ohmic resistance in the cell, which can be attributed to the solution and electrical resistances of the instrumental setup and cell components. $R_{sf}$ characterizes the behaviour in the mid-to-low-frequency range, which is ascribed to the surface film resistance. $R_{ct}$ highlights the charge transfer resistance of the LTO electrode-electrolyte interface in the high-frequency region. The Nyquist plots revealed reduced $R_{sf}$ and $R_{ct}$ for both F-LTO and Cl-LTO compared to that of bare LTO, which is consistent with the CV results discussed earlier. EIS and CV measurements suggest that the F, Cl-doped LTO electrode shows a faster Li insertion/extraction kinetics than the bare LTO electrode, which aligns with the C-rate capability tests. The polarization of the cells increased with the current density, as indicated by the open charge/discharge galvanostatic curves. However, F-LTO and Cl-LTO consistently exhibited lower polarization due to their less resistive interfaces. As a result, both F- or Cl-doped LTO-based electrodes offered improved intercalation properties, which supports the Li diffusion DFT calculations discussed later.

The electrochemical performance of both F-LTO and Cl-LTO was evaluated over 1,000 cycles at a rate of 10C in half-cells, as shown in Fig. 7(a). The composition of our LTO electrode has a higher concentration of electrode active materials (90 wt%) and a lower concentration of conductive additives (5 wt%) than the widely accepted conditions of LTO researches (70-80 wt% of LTO and 20-10 wt% of conductive agent), we are expecting that the effects of F and Cl substitutions will be emphasized and easier to observe. By using this configuration, we expect that the effects of F and Cl substitutions will be easier to observed. Notably, the cycling stability and capacity retention of the halide-ion-incorporated LTOs were significantly enhanced. In comparison, the bare LTO reference electrode displayed an unstable capacity, retaining only 55 % of its initial capacity. On the other hand, F-LTO and Cl-LTO maintained capacities of 88 % and 90 %, respectively. Even after 1,000 cycles, the F-LTO and Cl-LTO electrodes continued to deliver capacities exceeding 110 mAh $g^{-1}$, with Cl-LTO reaching around 120 mAh $g^{-1}$.

To explore the impact of halogen ion doping on cyclability, XPS analysis was performed on the cycled electrodes, as illustrated in Figs. 7(b) and (c). The Ti 2p and C 1s spectra of both F-LTO and Cl-LTO electrodes display surface chemistry that is relatively similar to that of the bare reference. A minor shift toward higher binding energies was detected for the Ti $2p_{3/2}$ peaks, which could be attributed to a more electronegative surface influenced by the halogen elements. The Ti 2p peaks also appeared slightly more intense, potentially indicating a thinner SEI formation on halide ion-doped LTO materials. This could be due to a decrease in surface reactivity resulting from the strength of ion bonding nature in comparison to oxides.[36] However, these subtle differences in SEI nature, particularly for LTO electrodes, are not sufficient to account for the observed electrochemical improvements.[44]

Fig. 7(d-f) presents the FE-SEM images of the LTO electrodes after the 1,000-cycle test. In contrast to graphite electrodes, a dense and stable SEI layer did not form on the surface of the LTO electrode. As a result, the electrolyte remains in direct contact with the LTO surface during the charge-discharge process, leading to continuous reductive decomposition at the surface and subsequent electrode swelling due to gas expansion. The FE-SEM images clearly show numerous cracks on the LTO electrode surface, while they are barely noticeable in the halogen-substituted LTOs. The reaction mechanism with the electrolyte on the LTO surface of LTO has been still largely unknown, in particular gas generation in the electrolyte has

been a particularly prominent issue. Previous studies have suggested that a reconstructed surface with partial desorption of oxygen atoms is formed on the LTO surface. Such oxygen vacancies are likely to cause electrophilic reactions to the species present in the electrolyte. The XAFS results shown in Fig. 5 revealed a significant decrease in the presence of pentacoordinate Ti atoms on the surface due to the halide bonding. According to the above all results, it is hypothesized that the significant improvement in the cycling characteristics of F-LTO and Cl-LTO may be attributed to the suppression of gas evolution reaction. However, it should be noted that the cycle characteristics of LTO may be slightly underestimated because the difference in the rate characteristics of LTO due to F and Cl substitution is also added to the capacity loss with respect to the number of cycles.

**DFT calculation: atomic structure**

DFT calculations were conducted to shed light on the doping-induced effects on the intrinsic structures and to investigate the correlation between morphological and electrical changes in F-LTO and Cl-LTO crystals. Two possible charge compensation mechanisms arise from the partial substitution of $O^{2-}$ with $F^-$ or $Cl^-$ in LTO: $Ti^{3+}$ formation via $Ti^{4+}$ reduction (mixed valence model) and $Li^+$ defect formation ($Li^+$-deficient model). For example, F-LTO (Cl-LTO) composition in a mixed-valence model is represented as $Li_4Ti_5O_{12-x}F_x$ ($Li_4Ti_5O_{12-x}Cl_x$), where $x$ ranges from 0.25 ($Li_4Ti_5O_{11.75}F_{0.25}$, $Li_4Ti_5O_{11.75}Cl_{0.25}$) to 1.0 ($Li_4Ti_5O_{11.00}F_{1.00}$, $Li_4Ti_5O_{11.75}Cl_{1.00}$) representing the amount of $F^-$ ($Cl^-$) substitution. Since the structural model (supercell) of LTO analysed in this study consists of $Li_{16}Ti_{20}O_{48}$, the substitutions of $x$ = 0.25, 0.50, 0.75, and 1.0 correspond to single-, double-, triple-, and quadruple-$F^-$ ($Cl^-$) substitutions in the supercell, respectively, based on the underlying spinel framework. Our findings emphasize that the halide anion prefers to substitute the $O^{2-}$ ion at the octahedral 32e site at the corner shared by $Li_{8a}$, Li16d, and two $Ti_{16d}$ ions, depending on the number of replacements. The most stable atomic arrangements of $F_{1.0}$-LTO and $Cl_{1.0}$-LTO are depicted in Fig. S11. This trend aligns well with a previous report.[41] In the mixed-valence model, it was discovered that $Ti^{4+}$ associated with coordinated $F^-$ or $Cl^-$ forms the oxidation state of $Ti^{3+}$ through charge compensation. The $Ti^{3+}$ generated by replacing $F^-$ ($Cl^-$) with $O^{2-}$ leads to significant distortion of the $TiO_6$ octahedron, while the adjacent $LiO_6$ octahedron helps to alleviate this distortion. This is thought to create a more energetically stable coordination environment compared to one surrounded by three $TiO_6$ octahedra. Additionally, the cell volume expands in relation to pristine LTO after doping with $F^-$ or $Cl^-$, a consequence of the larger ionic radius of $Ti^{3+}$ compared to $Ti^{4+}$. This expansion is likely to facilitate $Li^+$ diffusion by enlarging the channels within the LTO lattice (Fig. S12). In the $Li^+$-deficient model, $Li^+$ defects preferentially occupied the octahedral 16d sites over the tetrahedral 8a sites. This tendency was also observed when the number of $F^-$ ($Cl^-$) substituted atoms increased. This preference may result from stabilization due to the formation of strong Coulomb bonds, which arise from the shorter Li-O bond length at the tetrahedral site. As the substitution increased, cell volume shrinkage was observed in F-LTO, with the difference in ionic radii between $O^{2-}$ (1.40 Å) and $F^-$ (1.33 Å) predominantly contributing to lattice shrinkage. In contrast, cell volume expansion was observed in Cl-LTO with increasing substitution. The calculated formation energies for both models, pertaining to the reactions of LTO with LiF and LiCl, are summarized in Tables S1 and S2, respectively. In all cases, positive values were observed. This indicates that the halogen doping reaction does not proceed within the LTO lattice at the absolute temperature used in the DFT calculation. Moreover, charge compensation through $Li^+$ defect formation was found to be energetically more favourable than that via $Ti^{3+}$ formation. These calculated results do not align with the experimental outcomes, as $Ti^{3+}$ is evidently formed in the experiments with F-LTO and Cl-LTO.

The influence of temperature, particularly the chemical potential of oxygen gas, on the phase stability of each model, was examined, as the carbothermal reactions were carried out at 600 °C. Interestingly, by altering the chemical potential of oxygen gas, the $Ti^{3+}$ formation model became more dominant than the Li-deficient model. These results are summarized in Table S3. The DFT calculations reveal that the formation energies of the $Ti^{3+}$ structure model and the Li-deficient structure model are energetically equal at temperatures between 2100 and 2300 K under an oxygen partial pressure of 0.2 atm, above which the mixed valence model becomes more energetically favourable. In general, DFT calculations tend to overestimate thermodynamic parameters, such as temperature and pressure, when the effects of lattice vibrations at finite temperatures are not considered. Since temperature and lattice vibration were not accounted for in this study, it is reasonable to consider a temperature range of approximately 1500–1700 K, where the formation energies of both models are equal. In this work, the synthesis temperature of F-LTO and Cl-LTO was 973–1073 K, claiming $Ti^{3+}$ formation in the LTO lattice. It is highly plausible that mixed valence and Li-deficient models coexist in the F-LTO and Cl-LTO lattices. The carbothermal reactions of fluorination and chlorination at high temperatures may result in an energetic gain, promoting $Ti^{3+}$ formation.

**DFT calculation: surface energy and related morphological characteristics**

To explore the origins of facet truncation following halide ion doping, the surface energies of the {111}, {100}, and {110} facets were computed using DFT. A structural Segre model was prepared for both mixed valence and Li-deficient models, with halide ions segregating on the outermost surface of LTO. Tables S4 and S5 summarize the surface energies. The mixed-valence model of F-LTO exhibited higher surface energies than that of LTO, while the Li-deficient model demonstrated lower surface energies across all crystal planes, irrespective of the specific plane. This is attributed to the stability of $Ti^{4+}$, which exhibits a $3d_0$ electronic state. Regardless of the crystal facet, the surface structure reached its lowest energy when $F^-$ or Li defects simultaneously segregated on the outermost surface. The structural strain induced by $F^-$ substitution for $Li^+$ defects was

more effectively relaxed at the crystal surface compared to the bulk. Moreover, the surface energy of the {110} plane was the lowest, even though the LTO system showed the lowest surface energy for the {111} plane. In the case of Cl-LTO, the Li-deficient model's surface energy also tended to be smaller. However, both the {100} and {110} crystal planes displayed lower surface energies than LTO, even in the mixed-valence model. These findings indicate that halide ion substitution on the LTO surface influences morphological modifications by altering the relative stability of each exposed surface.

There are several possible reasons for the enhancement of the rate characteristics, we discussed the possibility of electronic and ionic diffusion characteristics contribution in this paper. Visual observation of the powders post-doping revealed that both F-LTO or Cl-LTO exhibited a slight blue hue, confirming the alteration of their band gaps. DFT calculations also detected significant changes in the electronic signature of LTO due to F or Cl doping. The calculated projected density of states (PDOS) for Ti3d are presented in Fig. 8(a) and (b). The original LTO's band gap was calculated to be around 2.0 eV, which is consistent with values found in the literature.[65, 66] The LTO band gap is primarily determined by the hybridization of O2p and Ti3d bands, as shown in Fig. S7(a) and (b). For mixed-valence F-LTO and Cl-LTO ($x$=1.0) models, a new intermediate Ti3d state emerged near the Fermi level, leading to a significant reduction in the band gap. The Fermi level (0 eV) shifted upward, reaching the newly generated intermediate state, indicating enhanced electronic conductivity. Simultaneously, the positions of all electronic PDOS shifted downward, aligning with n-type doping. Another approach to maintaining charge neutrality involves the formation of Li defects ($V'_{Li}$), which can be advantageous under controlled conditions.[67] The $V'_{Li}$ model's bandgap was estimated to be approximately 2.0 eV, nearly identical to that of LTO. This is because the charge compensation of halide ion substitution in the $V'_{Li}$ formation model does not produce $Ti^{3+}$. The electronic states of F-LTO and Cl-LTO varied significantly due to the charge-compensating reaction mechanism associated with halogen ion substitution. Even in halogen-doped LTOs, there is likely a difference in the extent to which battery performance improves due to halogen substitution. This discrepancy is attributed to the charge-compensating reaction mechanism determined by the doping conditions.

To investigate the impact of doping on Li-ion self-diffusion characteristics in LTO, we conducted DFT calculations to assess the activation barriers along conducive diffusion paths, as depicted in Fig. 8(c) and (d). This analysis was inspired by a previous study on F-doped LNMO cathode materials.[59, 60] The charge compensation effect resulting from both $F^-$ or $Cl^-$ doping was considered when analysing ion diffusion behaviour in both Li-deficient and mixed-valence model scenarios. All possible $Li^+/Ti^{4+}$ configuration models at the six octahedral 16d sites adjacent to the vacant octahedral 16c site in the $Li^+$ diffusion path was examined. However, since Li ions follow the most favourable path, we only listed the most favourable paths.

Energy profile analysis demonstrated that the $Li^+$ hopping pathway from the tetrahedral 8a site to the octahedral 16c site and then back to the tetrahedral 8a site was preferred. This pathway can be described by a symmetric transition state energy activation barrier (0.47 eV for pristine LTO). In contrast, the activation barrier appeared asymmetric from the starting $LiO_3F$ tetrahedral 8a site for all F-LTO models, due to the deformation of the bottleneck between the tetrahedral and octahedral sites (Fig. 8(c)). This may be attributed to the presence of slightly positive oxygen. The increase in site potential seems to result from the interaction between $Li^+$ and the 32e F site in the 8a-16c-8a route, which might contribute to the bottleneck deformation. The initial energy required increased by 0.1 eV and 0.2 eV for Li-deficient and mixed-valence models, respectively. Although the Li diffusion route was slightly modified, the transition state energy was reduced by $F^-$ doping to 0.39 eV and 0.24 eV for mixed-valence and Li-deficient models, respectively. This suggests that the energy barrier for $Li^+$ diffusion is not limited by the bottleneck deformation in F-LTO. In contrast, the Cl-LTO case (Fig. 8(d)) exhibited a higher activation barrier than bare LTO, and the Li diffusion routes were more affected. The larger atomic radius of chlorine compared to oxygen or fluorine caused significant deformation of the bottleneck region and increased the activation energy to 0.53 eV in the $Ti^{3+}$ model and 0.67 eV in the $Li^+$ defect model, respectively.

Our DFT calculations indicate that the increase in electronic conductivity due to the formation of $Ti^{3+}$ in Cl-LTO may be a major factor in the rate enhancement. On the other hand, in the case of F-LTO, charge compensation due to the formation of Li vacancies occurs preferentially rather than the formation of $Ti^{3+}$, indicating that ion diffusivity in the solid rather than electron conduction may strongly influence the rate characteristics.

Ceder *et al.* conducted a comprehensive investigation of $Li^+$ ion kinetic pathways in LTO and identified two primary factors that facilitate $Li^+$ diffusion. First, due to a smaller face-sharing number in the transition state, $Li^+$-$Li^+$ repulsion is thought to reduce the activation barrier. Second, local distortion decreases the coordination number of Li during migration through the three-coordinate oxygen face.[43] Therefore, F doping, by promoting $V'_{Li}$, enables the existence of a stable surface where $Li^+$-$Li^+$ repulsion is reduced and induces local distortion due to the electronegativity difference, resulting in a lowered activation barrier. It is important to note that these DFT calculations were performed for Li self-diffusion and did not consider LTO grain boundaries, which play a crucial role in the fast charge/discharge properties of Li.[68] However, experimental kinetic measurements support the benefits of F-LTO and provide a clear explanation of the impact of F-doping on the C-rate capability due to the enhancement of the Li diffusion coefficient.

## Conclusion

This study investigated the effect of incorporating fluorine and chlorine into LTO on its structural, electrical, and electrochemical properties, including the observation of enhanced capacity retention over 1,000 cycles at the rate of 10 C. Surface anion exchange induced by carbothermal

combustion reaction led to modifications in the surface properties without affecting LTO's zero-strain characteristics. Truncations of the 111 facets were observed after doping; these were explained through STEM observations, showing stabilization of the 100 faces. The calculated PDOS indicated that $F^-$ or $Cl^-$ doping improved conductivity, as evidenced by lowered conduction bands. Additionally, surface stability through the preservation of crystal neutrality was calculated through DFT-based quantum-mechanical atomistic simulations. The thermodynamics of two possible charge compensation reactions were simulated: $Li^+$-deficient ($V'_{Li}$) formation and surface reduction *via* $Ti^{3+}$ ($Ti^{4+}/Ti^{3+}$ mixed-valence state) formation. Calculations revealed that $Li^+$-deficient formation was favoured at absolute zero K for both F-LTO and Cl-LTO, whereas mixed-valence state formation was more likely favourable at high temperatures during the carbothermal reaction. Experimental XPS and STEM-EELS analyses also supported the conclusion that mixed-valence state formation was concentrated at the extreme surfaces of F-LTO and Cl-LTO particles. C-rate capacity tests, CV, and EIS measurements demonstrated enhanced kinetic parameters for both $Li^+$ diffusion and $Li^+$ exchange reactions at the electrolyte interface. To understand the self-diffusion characteristics of Li ions within the LTO framework, energy profiles along all kinetic pathways during $Li^+$ ion migration were further calculated using DFT. The initially poor diffusion properties of LTO were improved by F doping. The lowered activation barriers were attributed to the induced bottleneck deformation and reduced $Li^+$–$Li^+$ repulsion owing to the favoured Li defect formation. A better understanding of the influence of fluorine and chlorine, provided by the combination of theoretical DFT calculations and electrochemical tests, can lead to further optimization. Other important aspects, such as surface reactivity, namely SEI formation or outgassing issues, should also be investigated in the future. Pre-edge deconvolution analysis for T-K edge spectra revealed $F^-$ or $Cl^-$ doping on the LTO surface significantly reduced the presence of pentacoordinate Ti atoms due to halide bonding. It is hypothesized that the significant improvement in the cycling characteristics of F-LTO and Cl-LTO may be attributed to the suppression of gas evolution reaction. These novel insights offer new avenues for discovering high-rate electrode materials capable of delivering high cyclability.

## Author Contributions

N. Z. conceived of the presented idea. H. K. and D. K. designed and performed the experiments on the synthesis, characterization, and analyzation of the data. K. H. and H.S. designed the model and the computational framework and analyzed the data. Y. B-C assisted with XPS data analysis. R. I., G. S.S., and Y. I. carry out the STEM observation and EELS analysis. H. T. and E. O. carry out the XAS experiments and data analysis. K.T. partially supervised the project (JPMJCR1322). All authors discussed the results and contributed to the final manuscript. N. Z. wrote the manuscript in consultation with H. K., D.K, H. K., R. I., E. O. and Y. B-C.

## Conflicts of interest

The authors declare no conflict of interest.

## Acknowledgements

This work was partially supported by JST-CREST (JPMJCR21B3) and a Grant-in-Aid for Scientific Research (19H04693) from Japan. K.T. acknowledge JST-CREST (JPMJCR1322). GSS, RI, and YI acknowledge the Advanced Research Infrastructure for Materials and Nanotechnology Japan by MEXT.

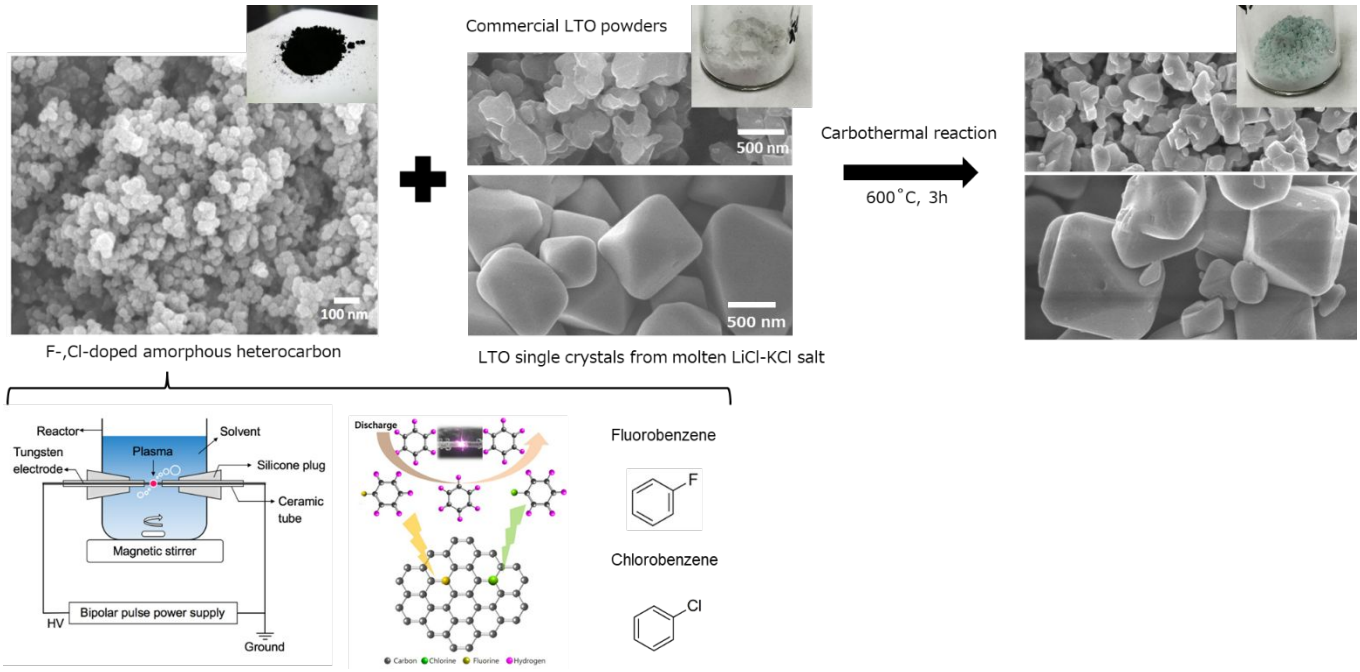


**Fig. 1** Schematics of $F^-$ or $Cl^-$ doped LTO preparation. Halide anion doping onto the LTO particle surface is achieved through a carbothermal reaction using $F^-$ or $Cl^-$ doped particles and LTO powders.

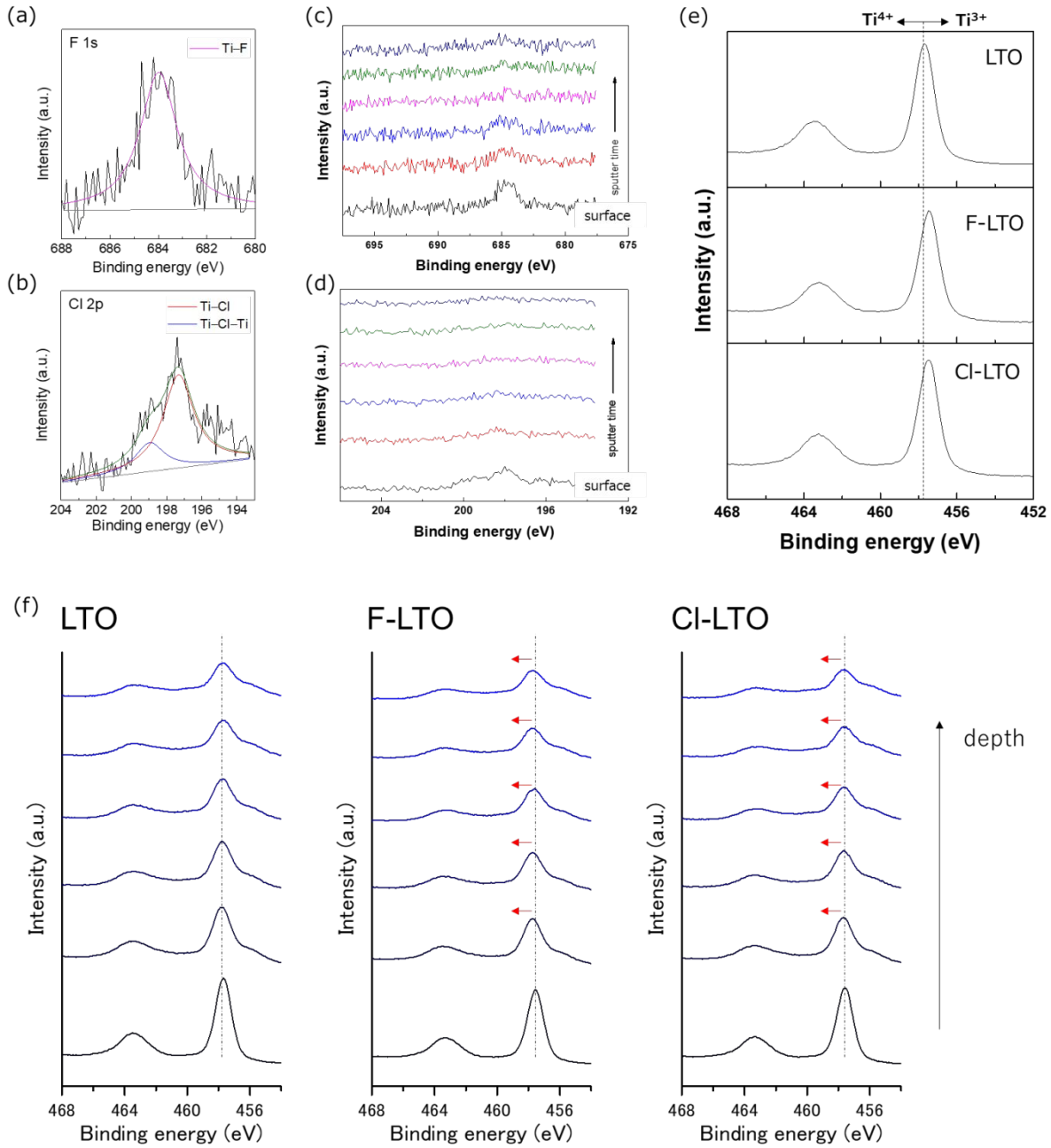


**Fig. 2** Identification of the chemical state changes of F, Cl, and Ti in $Li_4Ti_5O_{12}$ using X-ray photoelectron spectroscopy (XPS). (a) F 1s core-level spectra, (b) Cl 2p core-level spectra, (c) depth profile of F 1s core-level spectra, (d) depth profile of Cl 2p core-level spectra, (e) Ti 2p core-level spectra, and (f) depth profile of Ti 2p core-level spectra for LTO, F-LTO, and Cl-LTO. The etching thickness is maintained at 20 nm per Ar sputtering using a silicon wafer as a reference. The arrows in Figure 2 (f) are shown to clarify the peak shift.

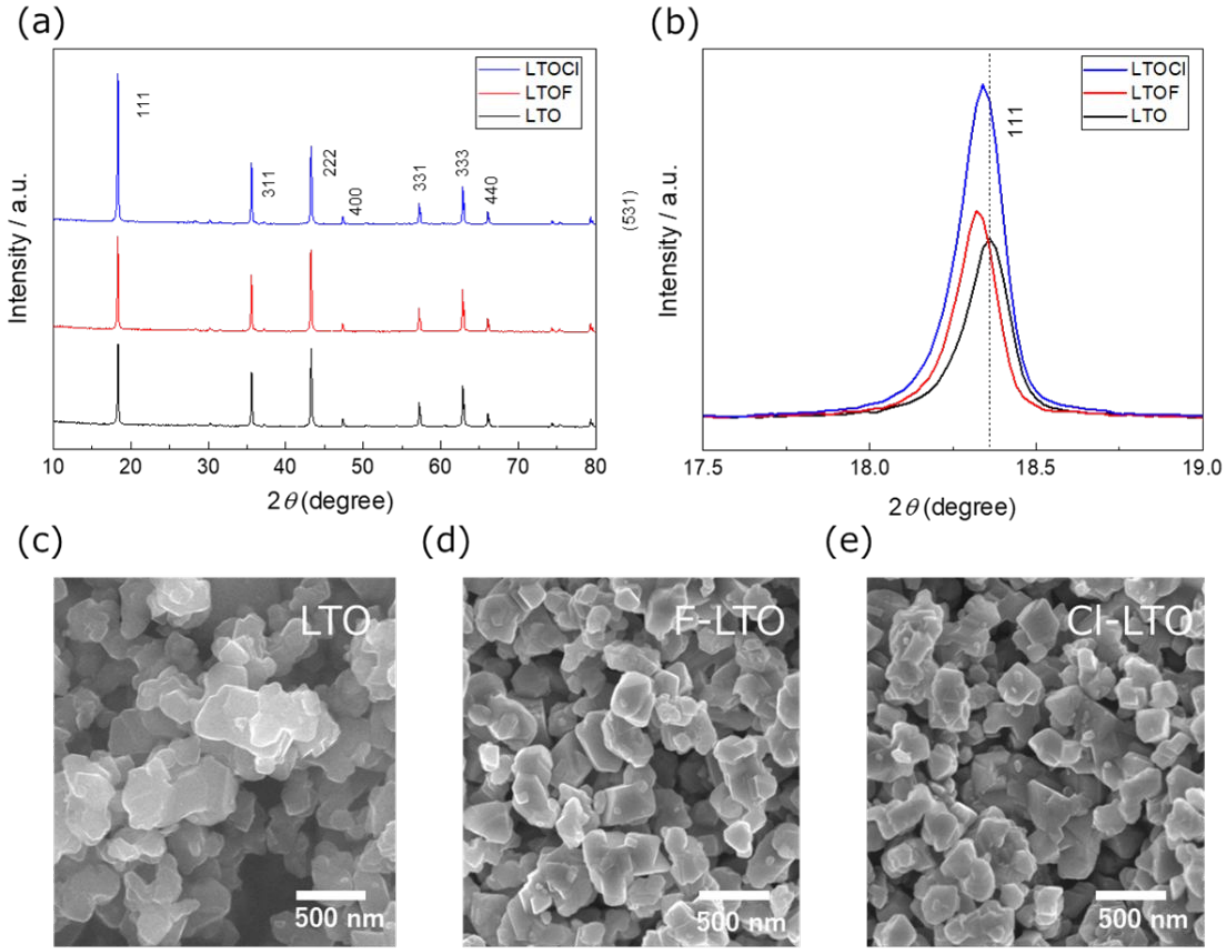


**Fig. 3** Effect of fluorine and chlorine anion incorporation on the lattice parameters of LTO. (a) Powder X-ray diffraction (XRD) patterns for LTO, F-LTO, and Cl-LTO particles, and (b) corresponding selected high-magnification XRD profiles ranging from 2θ of 17.5 to 19.0. (c)-(e) Field-emission scanning electron microscopy (FE-SEM) images of LTO, F-LTO, and Cl-LTO particles, respectively.

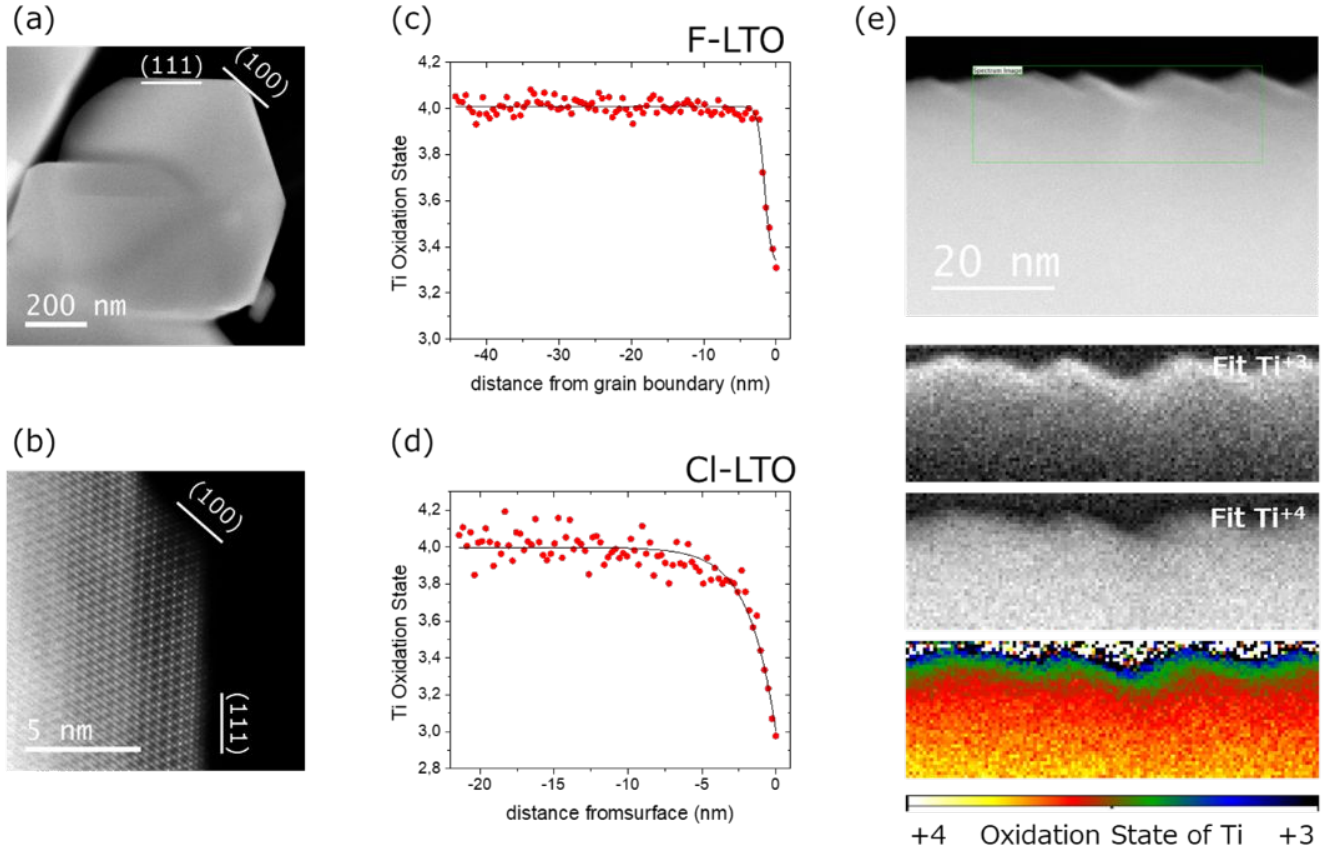


**Fig. 4** Surface atomic and electronic structures of halide anion doped LTOs characterized via scanning transmission electron microscopy (STEM). (a) and (b) show annular dark-field images of Cl-doped LTO, while (c) and (d) depict electron energy-loss spectroscopy (EELS) profiles (Ti-L2,3) obtained from the top surface and a depth of approximately 40 nm. Additionally, (e) presents a visualization of Ti oxidation states in Cl-LTO as a function of distance from the surface, using EELS Ti-L2,3 edges.

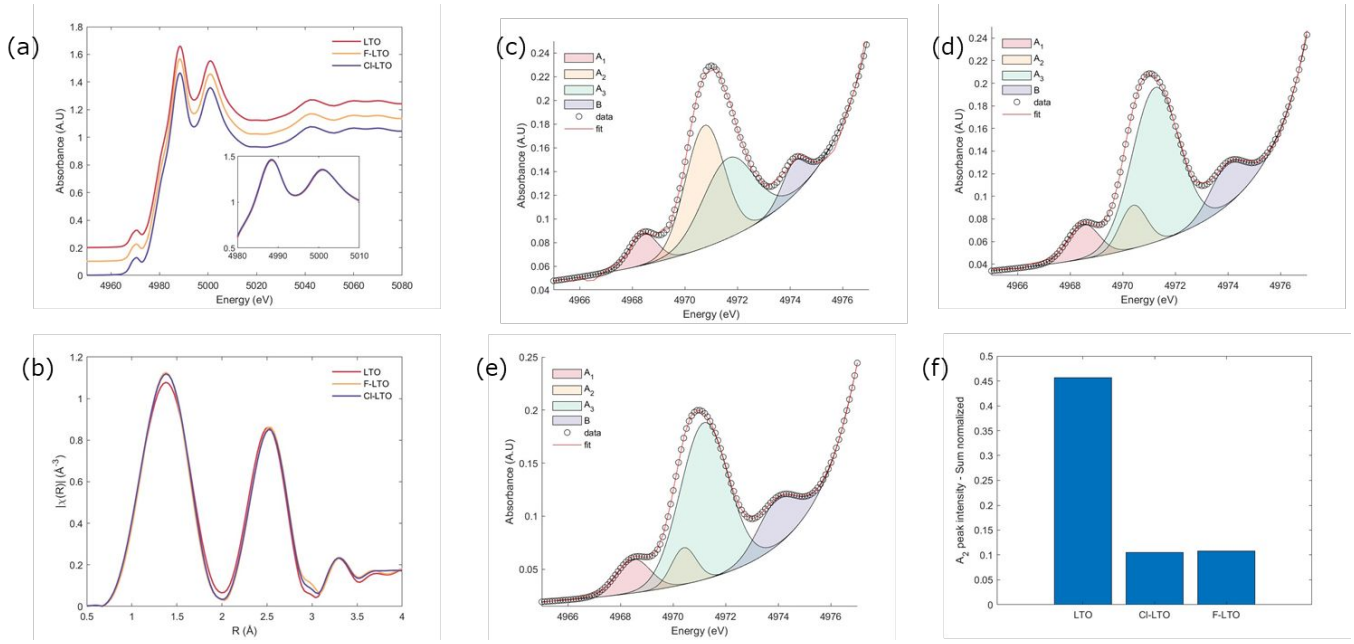


**Fig. 5** XAS analysis of LTO samples. (a) XANES spectra of LTO samples obtained in CEY, spectra are vertically shifted. Inset shows the same intensity of the white line. (b) Radial function distribution of LTO samples obtained in CEY. (c-e) Pre-edge deconvolution of LTO, Cl-LTO and F-LTO obtained in transmission mode. (f) A2 peak intensity for LTO samples.

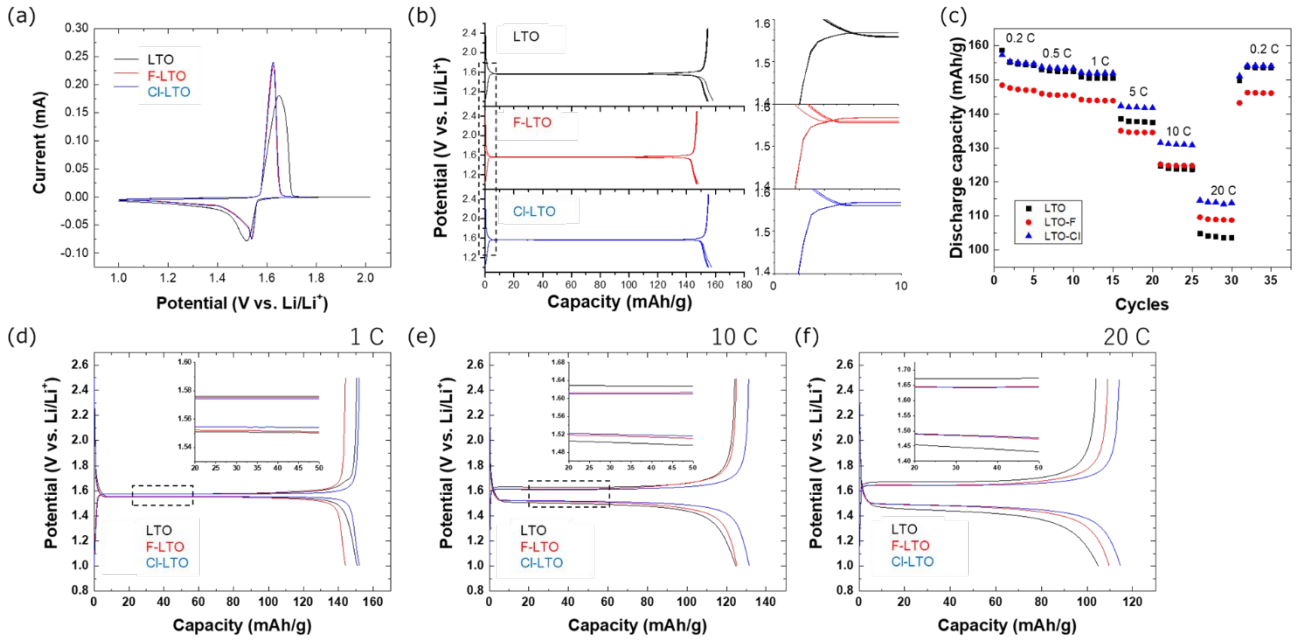


**Fig. 6** Electrochemical characterization of LTO electrodes with halides ion doping. (a) Cyclic voltammetry curves with a scan rate of 0.1 mV $s^{-1}$. (b) Galvanostatic charge-discharge profiles of LTO electrodes/Li cells at a 0.2 C rate, within a cut-off voltage range of 2.4-1.0 V ($Li^+$/Li). (c) C-rate capability test with rates ranging from 0.2 to 20C, operated under constant current (cc) mode. (d-f) Galvanostatic charge-discharge profiles of a series of LTO electrodes/Li cells at rates of 1, 10, and 20C.

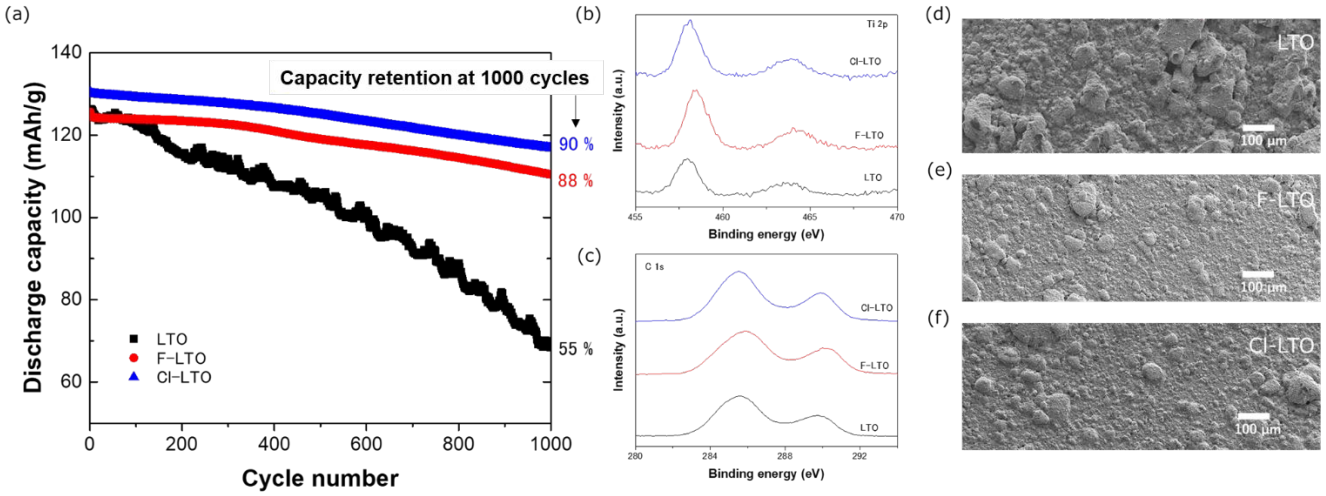


**Fig. 7** Effect of fluorine and chlorine anion incorporation on the cyclability of LTO electrodes. (a) Discharge capacity retention for pristine LTO, F-LTO, and Cl-LTO over 1,000 cycles at a 10C rate. (b, c) Ti 2p and C 1s core-level spectra obtained from the 1,000 cycled LTO, F-LTO, and Cl-LTO electrodes using X-ray photoelectron spectroscopy (XPS). (d-f) Field emission scanning electron microscopy (FE-SEM) images of the 1,000 cycled LTO, F-LTO, and Cl-LTO electrodes.

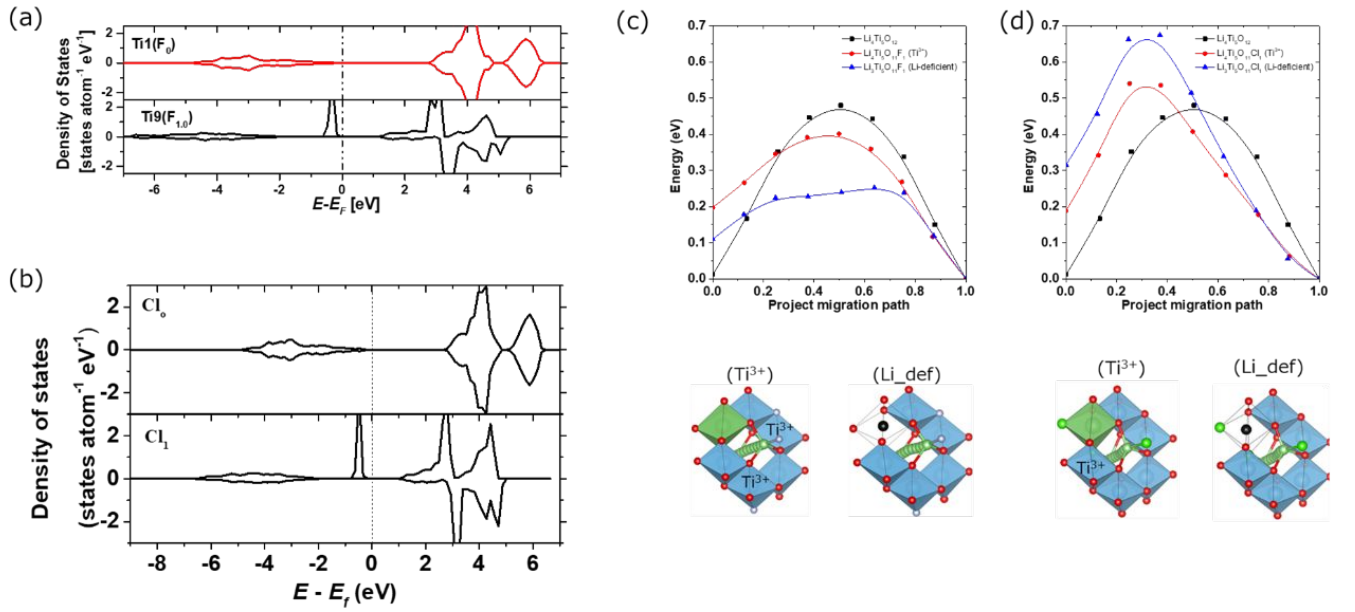


**Fig. 8** Effects of F- or Cl- doping on the electronic structure and self-diffusion characteristics. (a, b) Projected electronic density of states (PDOS) of $Li_4Ti_5O_{11}F_1$ and $Li_4Ti_5O_{11}Cl_1$, respectively, with F or Cl localized at the octahedral 32e site. (c, d) Energy profiles for $Li^+$ hopping along the most energetically favorable migration paths in the mixed valence model and $Li^+$ deficient model.

## Notes and references


1 Shen, C. et al.; Direct Observation of the Growth of Lithium Dendrites on Graphite Anodes by Operando EC-AFM. *Small Methods* **2**, 1–7 (2018).

2 Su, X. et al. Mechanisms for Lithium Nucleation and Dendrite Growth in Selected Carbon Allotropes. *Chem. Mater*. **29**, 6205–6213 (2017).

3 Yi, T.-F., Yang, S.-Y. & Xie, Y.; Recent advances of $Li_4Ti_5O_{12}$ as a promising next generation anode material for high power lithium-ion batteries. *J. Mater. Chem. A* **3**, 5750–5777 (2015).

4 Ohzuku, T., Ueda, A. & Yamamoto, N.; Zero‐Strain Insertion Material of $Li[Li_{1/3}Ti_{5/3}]O_4$ for Rechargeable Lithium Cells. J. Electrochem. Soc. 142, 1431‐1435 (1995).

5 Scharner, S., Weppner, W. & Schmid‐Beurmann, P.; Evidence of Two-Phase Formation upon Lithium Insertion into the $Li_{1.33}Ti_{1.67}O_4$ Spinel. J. Electrochem. Soc. 146, 857‐861 (1999).

6 Wagemaker, M. et al. A kinetic two-phase and equilibrium solid solution in spinel $Li_{4+x}Ti_5O_{12}$. Adv. Mater. 18, 3169–3173 (2006).

7 Ziebarth, B., Klinsmann, M., Eckl, T. Elsässer, C.; Lithium diffusion in the spinel phase $Li_4Ti_5O_{12}$ and in the rocksalt phase $Li_7Ti_5O_{12}$ of lithium titanate from first principles. Phys. Rev. B 89, 174301 (2014).

8 Wilkening, M., Amade, R., Iwaniak, W. & Heitjans, P. Ultraslow Li diffusion in spinel-type structured $Li_4Ti_5O_{12}$; A comparison of results from solid state NMR and impedance spectroscopy. Phys. Chem. Chem. Phys. 9, 1239–1246 (2007).

9 Hain, H. et al.; Study of local structure and Li dynamics in $Li_{4+x}Ti_5O_{12}$ ($0 \le x \le 5$) using $^6Li$ and $^7Li$ NMR spectroscopy. Solid State Nucl. Magn. Reson. 42, 9–16 (2012).

10 Schmidt, W. et al. Small change-great effect: Steep increase of Li ion dynamics in $Li_4Ti_5O_{12}$ at the early stages of chemical Li insertion. Chem. Mater. 27, 1740–1750 (2015).

11 Schmidt, W., Wilkening, M.; Discriminating the Mobile Ions from the Immobile Ones in $Li_{4+x}Ti_5O_{12}$ $^6Li$ NMR Reveals the Main Li+ Diffusion Pathway and Proposes a Refined Lithiation Mechanism. J. Phys. Chem. C 120, 11372–11381 (2016).

12 Alaboina, P. K. et al.; Nanoscale Porous Lithium Titanate Anode for Superior High Temperature Performance. ACS Appl. Mater. Interfaces 8, 12127–12133 (2016).

13 Huynh, L. T. N. et al.; Synthesis and electrochemical properties of $Li_4Ti_5O_{12}$. J. Chem. 2019, 1–23 (2019).

14 Chen, J., Yang, L., Fang, S., Hirano, S. I.,Tachibana, K.; Synthesis of hierarchical mesoporous nest-like $Li_4Ti_5O_{12}$ for high-rate lithium ion batteries. J. Power Sources 200, 59–66 (2012).

15 Li, H. & Zhou, H. Enhancing the performances of Li-ion batteries by carbon-coating: Present and future. Chem. Commun. 48, 1201–1217 (2012).

16 Rahman, M. M., Wang, J. Z., Hassan, M. F., Wexler, D. & Liu, H. K. Amorphous carbon coated high grain boundary density dual phase $Li_4Ti_5O_{12}$-$TiO_2$; A nanocomposite anode material for li-ion batteries. Adv. Energy Mater. 1, 212–220 (2011).

17 Kim, H. K., Bak, S. M. & Kim, K. B.; $Li_4Ti_5O_{12}$/reduced graphite oxide nano-hybrid material for high rate lithium-ion batteries. Electrochem. commun. 12, 1768–1771 (2010).

18 Uceda, M. et al.; Highly conductive NMP-free carbon-coated nano-lithium titanate/carbon composite electrodes via SBR-assisted electrophoretic deposition. Electrochim. Acta 299, 107–115 (2019).

19 Ji, S. et al.; Preparation and effects of Mg-doping on the electrochemical properties of spinel $Li_4Ti_5O_{12}$ as anode material for lithium ion battery. Mater. Chem. Phys. 123, 510–515 (2010).

20 Zhang, Q. et al.; Preparation and electrochemical properties of Ca-doped $Li_4Ti_5O_{12}$ as anode materials in lithium-ion battery. Electrochim. Acta 98, 146–152 (2013).

21 Yi, T. F. et al.;Improving the high rate performance of $Li_4Ti_5O_{12}$ through divalent zinc substitution. J. Power Sources 215, 258–265 (2012).

22 Song, H. et al.;Anomalous decrease in structural disorder due to charge redistribution in Cr-doped $Li_4Ti_5O_{12}$ negative-electrode materials for high-rate Li-ion batteries. Energy Environ. Sci. 5, 9903–9913 (2012).

23 Zhao, H. et al.; Structural and electrochemical characteristics of $Li_{4-x}Al_xTi_5O_{12}$ as anode material for lithium-ion batteries. Electrochim. Acta 53, 7079–7083 (2008).

24 Yi, T. F. et al.; High rate cycling performance of lanthanum-modified $Li_4Ti_5O_{12}$ anode materials for lithium-ion batteries. J. Power Sources 214, 220–226 (2012).

25 Hou, L. et al.; Zr-doped $Li_4Ti_5O_{12}$ anode materials with high specific capacity for lithium-ion batteries. J. Alloys Compd. 774, 38–45 (2019).

26 Yi, T. F. et al.; High-performance $Li_4Ti_{5-x}V_xO_{12}$ ($0 \le x \le 0.3$) as an anode material for secondary lithium-ion battery. Electrochim. Acta 54, 7464–7470 (2009).

27 Tian, B., Xiang, H., Zhang, L., Li, Z., Wang, H.; Niobium doped lithium titanate as a high rate anode material for Li-ion batteries. Electrochim. Acta 55, 5453–5458 (2010).

28 Wolfenstine, J., Allen, J. L.; Electrical conductivity and charge compensation in Ta doped $Li_4Ti_5O_{12}$. J. Power Sources 180, 582–585 (2008).

29 Yi, T. F. et al.; Advanced electrochemical properties of Mo-doped $Li_4Ti_5O_{12}$ anode material for power lithium ion battery. RSC Adv. 2, 3541–3547 (2012).

30 Qi, Y., Huang, Y., Jia, D., Bao, S. J. & Guo, Z. P. Preparation and characterization of novel spinel $Li_4Ti_5O_{12-x}Br_x$ anode materials. Electrochim. Acta 54, 4772–4776 (2009).

31 Zhao, L., Hu, Y. S., Li, H., Wang, Z. & Chen, L.; Porous $Li_4Ti_5O_{12}$ coated with N-doped carbon from ionic liquids for Li-ion batteries. Adv. Mater. 23, 1385–1388 (2011).

32 Huang, Y. et al.; Synthesis and electrochemical properties of spinel $Li_4Ti_5O_{12-x}Cl_x$ anode materials for lithium-ion batteries. in Journal of Solid State Electrochemistry vol. 16 2011–2016 (Springer, 2012).

33 Chen, Y. et al. Fluoride doping $Li_4Ti_5O_{12}$ nanosheets as anode materials for enhanced rate performance of lithium-ion batteries. J. Electroanal. Chem. 815, 123–129 (2018).

34 Zhao, Z., Xu, Y., Ji, M. & Zhang, H. Synthesis and electrochemical performance of F-doped $Li_4Ti_5O_{12}$ for lithium-ion batteries. Electrochim. Acta 109, 645–650 (2013).

35 Charles-Blin, Y. et al.; Atomic Layer Fluorination of the $Li_4Ti_5O_{12}$ Surface: A Multiprobing Survey. ACS Appl. Energy Mater. 2, 6681–6692 (2019).

36 Charles-Blin, Y. et al.; Surface atomic layer fluorination of $Li_4Ti_5O_{12}$: Investigation of the surface electrode reactivity and the outgassing behavior in LiBs. Appl. Surf. Sci. 527, 146834 (2020).

37 Noerochim, L., Sulaksono, R., Prabowo, R. S., Widyastuti, W., Susanti, D., Subhan, A., Idris, N. H. batteries 38, 1-12 (2023)

38 Chen, C. H. et al. Studies of Mg-Substituted $Li_{4-x}Mg_xTi_5O_{12}$ Spinel Electrodes ($0 \le x \le 1$) for Lithium Batteries. J. Electrochem. Soc. 148, A102 (2001).

39 Meng, W. W., Yan, B. L. & Xu, Y. J. A facile electrochemical modification route in molten salt for $Ti^{3+}$ self-doped spinel lithium titanate. Electrochim. Acta 279, 128–135 (2018).

40 Meng, W. W., Yan, B. L., Xu, Y. J. Scalable synthesis of $Ti^{3+}$ self-doped $Li_4Ti_5O_{12}$ microparticles as an improved performance anode material for Li-ion batteries. J. Alloys Compd. 788, 21–29 (2019).

41 Yan, H., Zhang, D., Qilu, Duo, X., Sheng, X. A review of spinel lithium titanate ($Li_4Ti_5O_{12}$) as electrode material for advanced energy storage devices. Ceramics International 47, 5870-5895 (2021)

42 Zhang, W. et al.; Kinetic pathways of ionic transport in fast-charging lithium titanate. Science 367, 1030–1034 (2020).
43 Kageyama, H., Hayashi, K., Maeda, K., Attfield, J. P., Hiroi, Z., Rondinelli, J. M., Poeppelmeier, K. R. Expanding frontiers in materials chemistry and physics with multiple anions. Nat. Comm., 9, 772 (2018).
44 Salvatore, K-L.; Solution-Based, Anion-Doping of $Li_4Ti_5O_{12}$ Nanoflowers for Lithium-Ion Battery Applications, Chem. Eur. J., 26, 9389-9402 (2020).
45 Rossi T. C. et al.; X-ray absorption linear dichroism at the Ti K edge of anatase $TiO_2$ single crystals, Phys. Rev. B, 100, 245207 1-11 (2019).
46 Sánchez-Santolino, G., et al.; Characterization of surface metallic states in $SrTiO_3$ by means of aberration corrected electron microscopy. Ultramicroscopy 127, 109–113 (2013).
47 G. Kresse, J. Furthmüller; Efficiency of ab-initio total energy calculations for metals and semiconductors using a plane-wave basis set. Comput. Mater. Sci. 6, 15–50 (1996).
48 G. Kresse, J. Furthmüller, Efficient interative schemes for ab initio total-energy calculations using a plane-wave basis set. Phys. Rev. B 54, 11169–11186 (1996).
49 J. P. Perdew, et al.; Restoring the Density-Gradient Expansion for Exchange in Solids and Surfaces. Phys. Rev. Lett. 100, 136406 (2008).
50 P. E. Blöchl, Projector augmented-wave method. Phys. Rev. B., 50, 17953–27 (1994).
51 A. Jain, G. Hautier, S. P. Ong, C. J. Moore, C. C. Fischer, K. A. Persson, G. Ceder, Formation enthalpies by mixing GGA and GGA +U calculations. Phys. Rev. B, 84, 66–11 (2011).
52 T. Mueller, G. Hautier, A. Jain, G. Ceder, Evaluation of Tavorite-Structured Cathode Materials for Lithium-Ion Batteries Using High-Throughput Computing. Chem. Mater. 23, 3854–3862 (2011).
53 G. Henkelman, H. Jonsson,; Improved tangent estimate in the nudged elastic band method for finding minimum energy paths and saddle points, J. Chem. Phys., 113, 9978-9985 (2000).
54 G. Henkelman, B. P. Uberuaga, H. Jonsson; A climbing image nudged elastic band method for finding saddle points and minimum energy paths, J. Chem. Phys., 113, 9901-9904 (2000).
55 H. Shiiba, M. Nakayama, M. Nogami, Solid State Ionics, 181, 994-1001 (2010).
56 Salvatore,K-L.; Solution-Based, Anion-Doping of $Li_4Ti_5O_{12}$ Nanoflowers for Lithium-Ion Battery Applications, Chem. Eur. J., 26, 9389-9402 (2020) .
57 J. Ma, C. Wang, S. Wroblewski,; Kinetic characteristics of mixed conductive electrodes for lithium ion batteries, J. Power Sources, 164, 849– 856 (2007).
58 Rossi T. C. et al.; X-ray absorption linear dichroism at the Ti K edge of anatase $TiO_2$ single crystals, *Phys. Rev. B*, **100**, 245207 1-11 (2019).
59 Kim, D. W. et al.; Full picture discovery for mixed-fluorine anion effects on high-voltage spinel lithium nickel manganese oxide cathodes. *NPG Asia Mater*. **9**, 9 (2017).
60 Kim, D., Shiiba, H., Teshima, K., Zettsu, N., $Li^+$ Storage and Transport in High-Voltage Spinel-Type $LiNi_{0.5}Mn_{1.5}O_4$ Codoped with $F^-$ and $Cu^{2+}$. Journal of Materials Chemistry A, 2023,11, 838-848.
61 Farges, F., Brown Jr, G. E., Rehr, J. J.; Ti K-edge XANES studies of Ti coordination and disorder in oxide compounds: Comparison between theory and experiment, Phys. Rev. B, 56, 1809–1819 (1997).
62 Ma, J., Wang, C., Wroblewski, S.; Kinetic characteristics of mixed conductive electrodes for lithium ion batteries, *J. Power Sources*, **164**, 849– 856 (2007).
63 Park, M., Zhang, X., Chung, M., Less, G. B., Sastry, A. M.; A review of conduction phenomena in Li-ion batteries, *J. Power Sources*, **195**, 7904 –7929 (2010).
64 Y. He, A. Muhetaer, J. Li, F. Wang, C. Liu, Q. Li, D. Xu,; Ultrathin $Li_4Ti_5O_{12}$ Nanosheet Based Hierarchical Microspheres for High-Rate and Long-Cycle Life Li-Ion Batteries, *Adv. Energy Mater*. **7**, 1700950 (2017).
65 Zhang, Q., Verde, M. G., Seo, J. K., Li, X. & Meng, Y. S. Structural and electrochemical properties of Gd-doped $Li_4Ti_5O_{12}$ as anode material with improved rate capability for lithium-ion batteries. *J. Power Sources* **280**, 355–362 (2015).
66 Wang, L. et al. Structural and Electrochemical Characteristics of Ca-Doped 'flower-like' $Li_4Ti_5O_{12}$ Motifs as High-Rate Anode Materials for Lithium-Ion Batteries. *Chem. Mater*. **30**, 671–684 (2018).
67 Xu, H. et al. Fabrication of $Li_4Ti_5O_{12}$-$TiO_2$ Nanosheets with Structural Defects as High-Rate and Long-Life Anodes for Lithium-Ion Batteries. *Sci. Rep*. **7**, 2960 (2017).
68 Schmidt, W. & Wilkening, M. Diffusion-induced $^7Li$ NMR spin-lattice relaxation of fully lithiated, mixed-conducting $Li_7Ti_5O_{12}$. *Solid State Ionics* **287**, 77–82 (2016).